Biological network growth in complex environments – a computational framework

Torsten Johann Paul[1], Philip Kollmannsberger[1]

[1] Center for Computational and Theoretical Biology, University of Würzburg, Campus Hubland Nord 32, Würzburg, Germany

* philip.kollmannsberger@uni-wuerzburg.de

Abstract

Spatial biological networks are abundant on all scales of life, from single cells to ecosystems, and perform various important functions including signal transmission and nutrient transport. These biological functions depend on the architecture of the network, which emerges as the result of a dynamic, feedback-driven developmental process. While cell behavior during growth can be genetically encoded, the resulting network structure depends on spatial constraints and tissue architecture. Since network growth is often difficult to observe experimentally, computer simulations can help to understand how local cell behavior determines the resulting network architecture. We present here a computational framework based on directional statistics to model network formation in space and time under arbitrary spatial constraints. Growth is described as a biased correlated random walk where direction and branching depend on the local environmental conditions and constraints, which are presented as 3D multilayer images. To demonstrate the application of our tool, we perform growth simulations of the osteocyte lacuno-canalicular system in bone and of the zebrafish sensory nervous system. Our generic framework might help to better understand how network patterns depend on spatial constraints, or to identify the biological cause of deviations from healthy network function.

Author summary

We present a novel modeling approach and computational implementation to better understand the development of spatial biological networks under the influence of external signals. Our tool allows to study the relationship between local biological growth parameters and the emerging macroscopic network function using simulations. This computational approach can generate plausible network graphs that take local feedback into account and provide a basis for comparative studies using graph-based methods.

Introduction

Complex biological networks such as the neural connectome are striking examples of large-scale functional structures arising from a locally controlled growth process [1,2]. The resulting network architecture is not only genetically determined, but depends on biological and physical interactions with the microenvironment during the growth process [3, 4]. In this context, evolution has shaped diverse spatial networks on all length scales, from the cytoskeletal network in cells [5], to multicellular networks such as the vascular system [6] or the osteocyte

lacuno-canalicular network [7], to macroscopic networks of slime molds [8], mycelia [9] and plants [10]. Sophisticated imaging techniques together with large-scale automated analysis provide increasingly detailed views of the architecture of biological networks, revealing e.g. how neurons are wired together in the brain [11]. After extracting the topological connectivity from such image data, quantitative methods from the physics of complex networks can be applied to compare different types of networks and to uncover common organizational principles [12–15]. To understand the functional role of networks in the context of evolution, however, it is not sufficient to characterize static network structure [1]: we need to be able to infer the dynamics of the underlying biological growth process that defines this structure.

This poses a major challenge, since the local dynamics of the growth process is in most cases not experimentally accessible, except for simple model systems. Here, computer simulations provide a solution: they allow to connect the observed patterns to the underlying process by performing *in-silico* experiments. Different hypotheses can be tested by systematically varying the local growth rules in the simulation and analyzing the resulting network patterns. Such a computational approach also helps to overcome an important limitation of network physics with respect to spatial networks: the properties of complex networks are often calculated with respect to canonical random graphs such as the Erdös-Renyi [16] or Watts-Strogatz model [17]. These models are defined by the topological structure in an adjacency matrix, but usually neglect spatial constraints [18, 19]. A generic model of network growth under spatial constraints would thus address two important problems: enabling a meaningful quantification of spatial network patterns, and linking the observed patterns to the underlying biological growth process.

The first computer simulation of spatial network development, published in 1967 [20], already included the role of active and repulsive cues. Since then, several more advanced approaches to model spatial network growth have been developed. One type of model implements network growth by formation of edges between pre-existing nodes in space [21, 22] and was e.g. used to develop large-scale models of branching neurons [23] or leaf vascular networks [24]. Another type of approach is based on growth processes emanating from predefined seed points with branching and merging and has been used to model neural network development [25, 26], fibrous materials [27] or the development of branching organ structures [28]. Most of these existing models are targeted towards a specific domain such as neural networks and synapse formation, or include only simplified interactions with the environment. The current state of modeling spatial network growth was recently summarized in [1], arguing that there is "a crucial lack of theoretical models".

The aim of this work is to develop a generic framework for biological network development in space and time under arbitrary spatial constraints. We propose a probabilistic agent-based model to describe individual growth processes as biased, correlated random motion with rules for branching, bifurcation, merging and termination. We apply mathematical concepts from directional statistics to describe the influence of external cues on the direction of individual growth processes without restricting the model by making too specific assumptions about these cues. Structural and geometric factors are obtained directly from real image data rather than formulated explicitly. The model is implemented as a computational framework that allows to perform simulations for diverse types of biological networks on all scales, and to monitor the evolving spatial structure and connectivity.

Materials and Methods

Growth Process

The elementary process of biological network formation is the outgrowth of new edges in space from existing nodes, such as cells. Each individual growth agent, for example a neuronal growth cone, randomly explores space and senses soluble signals as well as physical

cues and obstacles. This process can be formulated as a biased correlated random walk [29]: the movement of edges is *biased* by attractive or repulsive signals and structural cues, and *correlated* due to directional persistence of edge growth. Edges turn into trees if branching and/or bifurcations occur. Finally, if edges can join other edges and form new nodes, a connected network emerges. The elements of this discretized, agent-based formalization of spatial network development are summarized in Figure 1. In the following, we describe our mathematical approach for modeling the growth process.

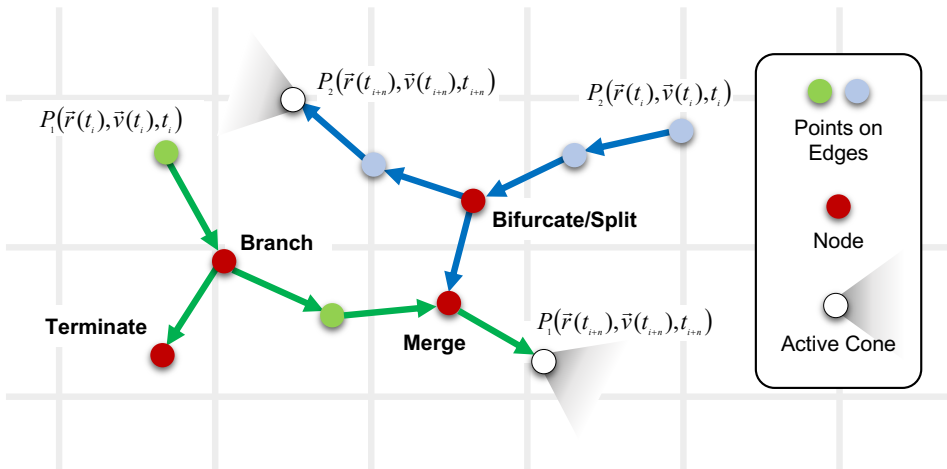

Fig 1. Discrete local events during spatial network development. Two growth agents (green and blue, e.g. growth cones, filopodia, cells) start at time t_i and randomly explore their environment in a biased correlated random walk. The environment is represented as a discrete grid (grey lines), while the network grows in continuous space. Blue and green dots correspond to subsequent positions of the growth cones. Cones can branch off new daughter cones, bifurcate/split in two new cones, merge with existing edges, or terminate. These events leads to formation of new nodes in the network, shown as red dots. Over time, the individual processes form a connected network of nodes and edges in space.

In its most general form, such a stochastic motion under the influence of external forces is described by the Fokker-Planck equation [30], corresponding to the Langevin equation [31]:

$$\frac{\delta p\left(\overrightarrow{x},t\right)}{\delta t} = -\nabla\left(\overrightarrow{u}\,p\left(\overrightarrow{x},t\right)\right) + \nabla\left(\mathbf{D}\nabla p\left(\overrightarrow{x},t\right)\right) \tag{1}$$

Equation 1 is a drift-diffusion equation of motion where the k-dimensional vector $\overrightarrow{u}(\overrightarrow{x},t)$ is a drift, and **D** the anisotropic and diagonal, $k \times k$- dimensional diffusion tensor. If drift and diffusion both are constant in time and space, and if the initial condition $p(\overrightarrow{x},0)$ is the k-dimensional Dirac delta function, then Equation 1 solves to

$$p\left(\overrightarrow{x},t\right) = \frac{1}{\sqrt{(4\pi)^k\,\mathbf{D}t}}\exp\left(-\frac{\left(\overrightarrow{x}-\overrightarrow{u}t\right)^2}{4\mathbf{D}t}\right) \tag{2}$$

Equation 2 describes the time development of a random movement for constant drift and isotropic diffusion. In a complex environment, however, both drift and diffusion can depend on time and position, and there is no simple analytic solution for the time development. In this case, a numerical approach can be taken by sampling individual movement traces as non-Markovian correlated processes [32]. The drift-diffusion movement is then discretized into a stepwise process where for each growth step, a new direction is drawn from a

probability density function (PDF). For constant drift and isotropic diffusion (Equation 2), the corresponding PDF, or growth kernel, is an isotropic multivariate Gaussian distribution with mean vector **u** and covariance **D**. In the general case, every discrete growth step has a different time- and position dependent PDF that encodes all spatial signals and constraints and from which the subsequent growth direction is drawn.

External Signals

The individual PDFs that describe the different internal and external cues can be formulated using the Multivariate Gaussian Distribution (MGD) as kernel:

$$g\left(\overrightarrow{x}, \overrightarrow{\mu}, \Sigma\right) = \frac{1}{\sqrt{(2\pi)^k \left|\Sigma\right|}} \exp\left[-\frac{1}{2}\left(\overrightarrow{x} - \overrightarrow{\mu}\right)^T \Sigma^{-1} \left(\overrightarrow{x} - \overrightarrow{\mu}\right)\right] \tag{3}$$

The MGD is a probability density function from which random vectors $\overrightarrow{X} \sim N\left(\overrightarrow{\mu}, \Sigma\right)$ of dimension k can be drawn that are shifted by the mean vector $\overrightarrow{\mu}$ and anisotropically distributed. The anisotropic distribution of directions is described by the metric of the $k \times k$ covariance matrix Σ with determinate $|\Sigma|$, eigenvectors $\overrightarrow{v}_1, .., \overrightarrow{v}_k$ and eigenvalues $\lambda_1, .., \lambda_k$. Depending on the edge's current position $\overrightarrow{p}$, the mean vector $\overrightarrow{\mu}$ points to the most likely direction, while the covariance Σ reflects the structure of the complex environment.

Following the mathematical rules for distributions, the PDF of a random vector that is the sum of independent random vectors is the convolution of the PDFs of the individual random vectors:

$$\mathrm{PDF}_{\mathrm{conv}} = \mathrm{PDF}_0 * ... * \mathrm{PDF}_{n-1} * \mathrm{PDF}_n \tag{4}$$

All local, external signals and structural properties that are described by individual PDFs in the form of a MGD can thus be combined into a single PDF that still has the form of a MGD [33]. As a result, a new growth direction that includes the contribution of all external cues can be drawn from this combined MGD with mean vector

$$\overrightarrow{\mu}_{\mathrm{conv}} = \sum_{i=0}^{n} \overrightarrow{\mu}_i \tag{5}$$

and covariance

$$\Sigma_{\mathrm{conv}} = \sum_{i=0}^{n} \Sigma_i \tag{6}$$

The parameter pairs $(\overrightarrow{\mu}_i, \Sigma_i)$ can represent different external cues, the geometry of the substrate, as well as edge-specific properties. In Table 1, we give some examples of external and internal cues and the structure of the environment that can be represented by such "Mean Vector - Covariance" pairs. For the case of a constant external vector field, the mean vector points towards the local field orientation, while its length scales with the field's strength. Its corresponding covariance is symmetric, proportional to the unit matrix $\mathbb{I}$, and the entries tend to zero ($\sigma_{1,\ldots,i} \to 0$). The MGD is then a k-dimensional delta distribution that biases the growing edge in the direction of the vector field. Diffusive external cues, such as the presence of signalling molecules, are treated in the same way: the mean vector points in the direction of increasing molecule density, or vice versa for inhibiting signals. This direction is calculated from the averaged motion of each ensemble of m particles. The diffusive covariances of all signaling particles are combined. Internal signals describe the properties of the growing edge, reflecting its characteristic random motion and its stiffness

or persistence. The physical interaction with the substrate is encoded in the structure tensor and the local derivatives (gradients) of the surroundings. The structure tensor takes the place of the diffusive tensor in the MGD, while the mean vector is the local gradient $\overrightarrow{\nabla} p\,(x, y, z)$. This concept, which is widely used in image analysis (e.g. anisotropic diffusion) [34–36], allows to include arbitrary structural information by representing it as an image volume and calculating the corresponding structure tensor.

Table 1. Mean Vector - Covariance pairs

External Cue	$\overrightarrow{\mu}$	Σ
Drift	$\overrightarrow{D}\left(\overrightarrow{p}\,(x, y, z)\right)$	$\sigma_{x,y,z} \to 0$
Signaling molecules	$\pm \sum_m^n \frac{\left(\overrightarrow{p}^s_{m,i} - \overrightarrow{p}^s_{m,i-1}\right)}{n}$	$\sum_m^n \Sigma_m$
Internal Cue	$\overrightarrow{\mu}$	Σ
RW - Random Walk	$\overrightarrow{0}$	diagonal, $\sigma_{x,y,z} > 0$
P - Persistence	$\sum_{i=m}^n \overrightarrow{p}_i$	isotropic, diagonal, $\sigma_{x,y,z} > 0$
Structural Cue	$\overrightarrow{\mu}$	Σ
Structure tensors	$\overrightarrow{\nabla} p\,(x, y, z)$	$\Sigma = \alpha R^T \Sigma^{dual}_{diag} R$ $\Sigma_{diag} = R \Sigma_{i,j} R^T$ $\Sigma_{i,j} = \delta_i p \delta_j p$ $i, j \in (x, y, z)$

Table 1: Examples how external, internal and structural cues interact with a growing edge at position $\overrightarrow{p}$ in 3D. The physical properties are interpreted as multivariate Gaussian distributions with a mean vector $\overrightarrow{\mu}$ and covariance Σ. All signals are combined into a single PDF by convolution. We distinguish between external signals such as drift and signaling cues, internal properties of an edge such as its random motion and stiffness, and the structural properties of the surroundings.

The combination of the different PDFs through convolution (Equation 4) results in a single MGD from which the subsequent growth direction is drawn. This combined PDF distributes random vectors around a mean vector with a length that is the sum of all mean vectors of the individual signals. The shape of this shifted multivariate normal is expressed by its covariance.

Step Length

In general, growth direction and step length are independent from each other. To separate the growth direction from the step length, the PDF needs to be projected onto a sphere. Distributions on the unit sphere $\mathbb{S}^{k-1}$ can be obtained by embedding $\mathbb{S}^{k-1}$ in $\mathbb{R}^k$. For a random vector $\overrightarrow{x} \in \mathbb{R}^k$, this could be its conditional distribution on $\|\overrightarrow{x}\| = 1$, or its angular projection $\overrightarrow{y} = \overrightarrow{x}/\|\overrightarrow{x}\|$. For the family of Fisher-Bingham distributions [37], the Bingham distribution [38] is the conditional distribution, while the Kent distribution is the projection of the general Fisher-Bingham distribution [39]. Although these distributions are well studied and are commonly used for data fitting and directional statistics [40], the Kent distribution is not suitable for simulations, as it requires a rejection method [41]. Instead, the MGD can be transformed to spherical coordinates, which allows to calculate a spherical marginal distribution $\text{MGD}_{\text{angular}}$ by integrating over the radial component to obtain a projection of

the MGD . Starting from Equation 3, the k-dimensional coordinate basis is transformed to $\overrightarrow{x} = r\overrightarrow{y}$ with $r = \|\overrightarrow{x}\|$, $\overrightarrow{y} = \overrightarrow{x}/\|\overrightarrow{x}\|$ and $d\overrightarrow{x} = r^{k-1}drd\overrightarrow{y}$. The transformation and integration of Equation 3 results in the following angular MGD:

$$MGD_{\text{angular}}\left(\overrightarrow{y}\right) = \int_{0}^{-\infty} MGD\left(r, \overrightarrow{y}\right) r^{k-1} dr \tag{7}$$

Carrying out the integration yields the general angular Gaussian distribution (GAGD), introduced and explicit calculated for dimensions $k = 1, 2, 3$ in [42], which is the angular marginal distribution to the MGD that projects the directional probability information onto the $\mathbb{S}^{k-1}$-sphere:

$$\begin{aligned} MGD_{angular}\left(\overrightarrow{y}\right) = & \frac{1}{\sqrt{(2\pi)^{(k-1)}\left|\Sigma\right|}} \frac{1}{\sqrt{\overrightarrow{y}^T \Sigma^{-1} \overrightarrow{y}}} \\ & \times \exp\left[\frac{1}{2}\left(\frac{\left(\overrightarrow{y}^T \Sigma^{-1} \overrightarrow{\mu}\right)^2}{\overrightarrow{y}^T \Sigma^{-1} \overrightarrow{y}} - \overrightarrow{\mu}^T \Sigma^{-1} \overrightarrow{\mu}\right)\right] \\ & \times M_{k-1}\left(\frac{\overrightarrow{y}^T \Sigma^{-1} \overrightarrow{\mu}}{\sqrt{\overrightarrow{y}^T \Sigma^{-1} \overrightarrow{y}}}\right) \end{aligned} \tag{8}$$

The last term $M_{k-1}\left(\frac{\overrightarrow{y}^T \Sigma^{-1} \overrightarrow{\mu}}{\sqrt{\overrightarrow{y}^T \Sigma^{-1} \overrightarrow{y}}}\right)$ of Equation 8 is a function

$$\begin{aligned} M_{k-1}\left(\alpha\right) = & \\ & \int_{u=0}^{\infty} u^{k-1} \frac{1}{\sqrt{2\pi}} \exp\left(-\frac{\left(u-\alpha\right)^2}{2}\right) du \end{aligned} \tag{9}$$

For the 3-dimensional case $k = 3$, $\overrightarrow{y}^T = (\sin\theta\cos\phi, \sin\theta\sin\phi, \cos\theta)$, this results in

$$M_2\left(\alpha\right) = \left(1 + \alpha^2\right)\Phi\left(\alpha\right) + \alpha\phi\left(\alpha\right)$$

where $\phi\left(.\right)$ is the standard normal PDF and $\Phi\left(.\right)$ the corresponding CDF, the cumulative distribution function.

This definition separates the radial distribution from the angular distribution. While we use a constant step length in our simulations, this separation would also allow for variable step length PDFs without losing any information of the spatial distribution of external cues with large mean vectors $\overrightarrow{\mu}$. In Figure 2, we show three distributions on the unit sphere $\mathbb{S}^{k-1} \in \mathbb{R}^k$ for three dimensions with different mean vector $\overrightarrow{\mu}$ and covariance Σ as examples for shifted isotropic signals (persistence), highly anisotropic covariances due to spatial constraints such as edges and walls, and peaked distributions for guidance cues towards specific directions. The structural information is projected onto the unit sphere while retaining the full information about Σ and μ, as shown in Equation 8 – e.g., a bimodal MGD still retains a bimodal marginal $\text{MGD}_{\text{angular}}$ due to its covariance.

After motivating the mathematical kernel for the growth process and the interaction with the substrate, we now introduce the rules that enable the growing edges to bifurcate, branch off daughter processes, to form new connections (e.g. synapses) with other edges, and to be persistent and locally self-avoiding.

Persistence

During edge outgrowth, the finite bending stiffness of edges causes the growth direction to be correlated to the previous directions, resulting in persistence of the movement. In absence

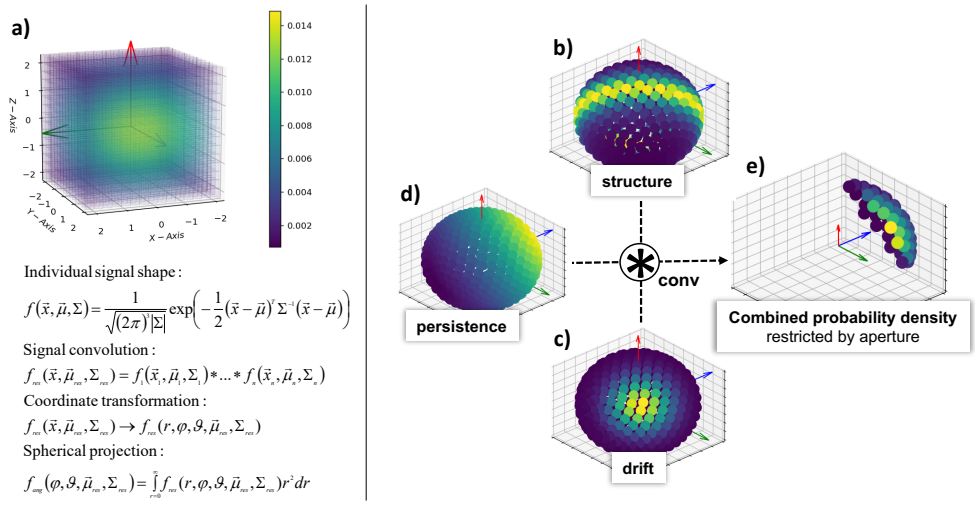

Fig 2. Probabilistic framework to determine the next growth direction. Probability distributions are modeled as multivariate Gaussian distributions (MGD), shown in a), with mean and covariance determined from the discrete simulation grid that describes structural and soluble cues. Individual MGDs are combined by convolution, transformed to spherical coordinates, and projected onto the unit sphere (bottom). Examples shown on the right hand side include structural guidance along a plane (e.g. a tissue boundary, b), a unidirectional drift towards the viewer (e.g. a growth factor gradient, c), and persistence due to memory of past growth directions (e.g. bending stiffness, d). The three probability distributions are merged by convolution, restricted by the aperture of the growth cone, and sampled on the corresponding segment of the sphere (e). The next growth direction is drawn from this combined, restricted distribution.

of a drift vector $\overrightarrow{\mu}$, and since the eigenvectors of the covariance matrix Σ are independent, the random growth process is a Wiener and Markov Process, and still remains a general interpretation of a Wiener process for $\|\overrightarrow{\mu}\| > 0$. Persistence of the growth direction is equivalent to introducing a drift that is the sum of the last t growth directions $\overrightarrow{\mu}_P = \sum_i^t \overrightarrow{\mu}_i$. This results in an effective bending stiffness of the growing edges, and its persistence length is expressed by the Kuhn length [43],

$$P_{\mathrm{Kuhn},t} = \lim_{\delta L \to \infty} \delta L \sum_{j=i+1}^{t} < \cos\theta_{i,j} >, \tag{10}$$

where δl is the length between two steps and $\delta l < \cos\theta_{i,j} >$ is the projected length at i towards j (Figure 1). This directional correlation does however not imply self-avoidance within the persistence length scale, as there still is a non-zero probability for an edge to loop back and collide with itself within the persistence length.

Self Avoidance

Local self-avoidance is achieved by restricting possible growth directions to a solid angle Ω around $\overrightarrow{\mu}_{\mathrm{P}}$. The aperture described by Ω is equivalent to the maximum allowed curvature of a growing edge. This means that the heuristic growth process is no longer a Markov process [44], as it loses its reversibility, but now becomes self avoiding within the persistence length. Figure 2 shows the effect of persistence on the angular distribution MGD_{angular} and how the aperture is restricted by Ω.

Connectivity

New nodes in a growing network form by branching or bifurcation of growing edges, or when a growing edge merges with another edge. We distinguish between "branching", the branching-off of a new edge from a growing edge where the parent edge maintains its growth direction, and "bifurcation", the splitting of a growing edge into two daughter edges growing in two different directions. Both can occur at every growth step with a probability that depends on edge properties (e.g. age) as well as external cues. Whenever an edge is within a certain distance to another edge, it can merge and form a new node, again with a probability that can depend on edge properties and external signals. Finally, growing edges can terminate and form an end-node, again with a probability that depends on external signals, such as obstacles or the density of already existing edges. Figure 1 schematically shows the time development of a growing network where edges branch several times, merge, and terminate.

Implementation

We next describe the computational implementation of the theoretical framework for spatial network growth described in the previous sections. Key input parameters for the simulation are the spatial environment and the seed points (e.g. cells) that define from where the first edges start to grow. The spatial environment is provided in the form of 3D image volumes that contain information about the physical structure of the growth environment (e.g. tissue structure), as well as about signals that influence the growth process (e.g. growth factors). This allows to study network growth in real tissue environments, as measured e.g. with confocal or light sheet microscopy. Besides these image data and the seed points, the simulation requires a number of model parameters such as step length, aperture and degree of persistence as input, listed in Table 2.

Table 2. Simulation parameters

Internal Parameter	**Default Value**
Aperture Ω	$\Omega = 25$ deg
Step size s	$l \in \mathbb{R}$, $l \sim f(\mu, \sigma)$
Splitting angle	$\theta_{bran} = 75$ deg, $\theta_{bif} = 75$ deg
Search field	3x3x3 cube
Probabilities	$p_{bran} = 2\%$, $p_{bif} = 5\%$, $p_{term} = p_{reac} = 0.01\%$
Memory	m = 5
External Parameter	**Default Value**
Instances	i = 10
Steps	s = 25
Cone, Edge, Node number	c,e,n = 100000 (max. object counter)
MGD Switches	Boolean
Start seed parameter	X, Y, Z, ϕ, θ

Table 2: List of parameters of the implementation and their default values

The PDFs for the growth processes are derived from the image volumes by calculating gradients and the structure tensor (Figure 3). These image volumes can contain multiple channels to describe not only structure, but also scalar and vector fields to describe forces or signaling particles. The spatial growth environment can also be dynamic, either via external

time-dependent changes or via changes introduced by the growing network itself. Notably, it is by this reciprocal feedback between the growing network and its spatial environment that the network architecture turns into an emergent property that cannot be encoded in the growth rules alone.

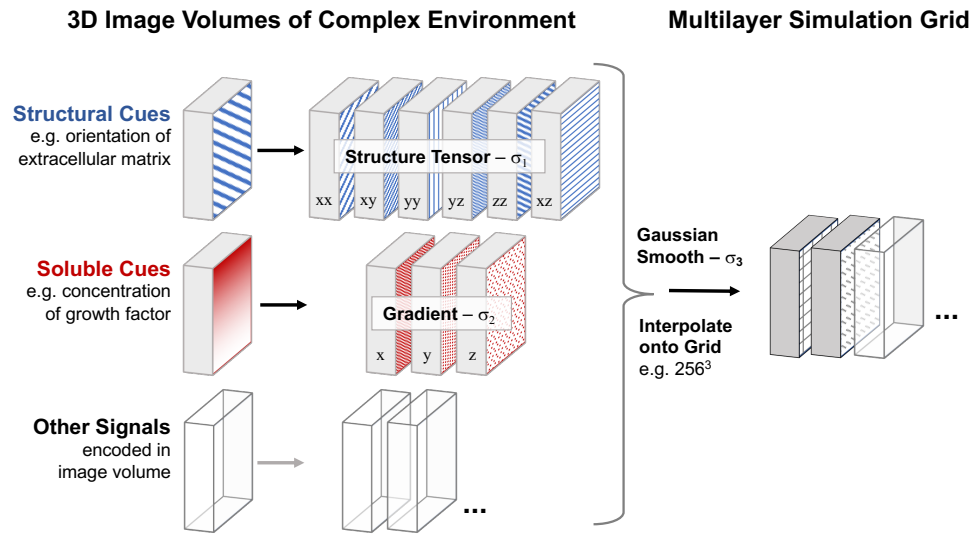

Fig 3. Mapping the complex growth environment onto a multilayer simulation grid. Structural and soluble cues and other signals are provided as 3D image volumes of real or simulated data (left). The six components of the structure tensor define the guidance cues from the substrate structure, whereas the three gradients of the images of soluble cues, e.g. growth factor concentrations, define the resulting directional bias. The feature sizes σ_i used for the filters determine the resolution of the cues. Other signals can be integrated by computing the corresponding features (filters) that define the resulting growth cue. The image features containing the different cues are Gaussian smoothed and interpolated onto the final simulation grid. The growth simulation uses continuous coordinates on a discrete grid.

The growing edges are implemented as instances of a growth cone class with the properties listed in Table 3. These include both internal parameters as well as functions that define how external cues are translated into growth directions. All object instances work on internal memories, are able to create new objects, and can inherit their parameters. The workflow and interaction of the different memories are summarized in Figure 4.

Prior to deciding on the growth direction according to Equation 8, the agent checks if there is a merge, branch, bifurcation or termination event. For merging, the agent performs a collision detection with radius R_c over all edges E_n of an ensemble Ω_E that includes all edges within a cluster specified through its members that can interact during t growth steps. A new node is created at the ith positions $\overrightarrow{P}_{i,j}$ of the jth edge $j \in \Omega_E$ that fulfils the condition

$$|\overrightarrow{P}_{agent} - \overrightarrow{P}_{E_n}|^2 \leq (2R_c)^2. \tag{11}$$

The cone terminates afterwards and the memory attributes of all participating objects are updated. Branching and bifurcation are executed via object functions. The events occur randomly with their respective probability. This probability and the parameters for branching angle and direction as well as the bifurcation plane are coupled to the external parameters of the spatial environment. The same type of coupling is implemented for termination and

Table 3. Growth cone attributes and actions

Attribute	**Type**
Positions	array $[[x, y, z]_i, .., [x, y, z]_n]$
Spherical angles	array $[[\phi, \theta]_i, .., [\phi, \theta]_n]$
First and last node	list(str)
Current Node and Edge	int
Current state	str
Action	**Description**
Growth	Construct $\text{MGD}_{ang}(\overrightarrow{\mu}, \Sigma)$, draw next direction
Branch	Create new cone object at an angle
Bifurcate/Split	Creates two new cone objects at an angle
Merge	Merge current edge with nearby edge
Terminate/Reactivate	Inactivate/reactivate cone

Table 3: Internal attributes and functionality of growth cone objects.

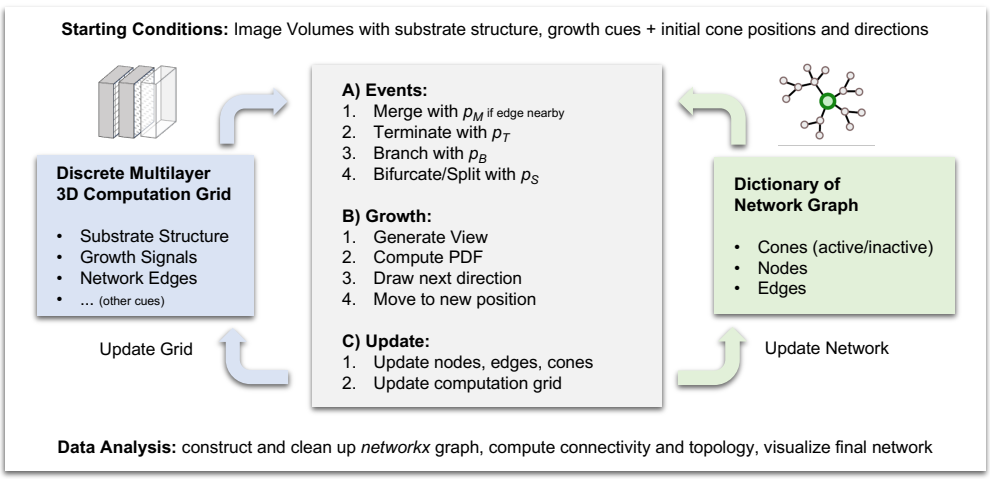

Fig 4. Diagram of the simulation. Starting conditions are provided as image volumes and as list of initial positions and directions. During each time step, the steps in the grey box are performed in parallel for each cone. The four elementary event types during network growth occur with their respective probabilities (A), depending on the local environment. Afterwards, the next position of each cone is determined from the spherical probability distribution computed from the local environment (B). Finally, the computation grid (left) and network dictionary (right), which are kept in shared memory, are updated by each parallel process, such that they can provide up-to-date conditions for all cones in the subsequent step. Finally, the network graph is constructed, its topological properties computed, and the network is visualized. These analysis steps can also be performed periodically during the simulation to monitor network development on-the-fly.

reactivation processes. If an agent branches or bifurcates, a new node is created at the splitting position. In the case of branching, a new cone object emerges from the new edge, and the mother branch updates its memory. For bifurcation, the old cone terminates, and

two or more new cone objects are created and grow in new directions with an oblique angle to each other.

As the framework relies heavily on the communication of all objects, an efficient parallelization strategy is important. Already existing edges are not only stored in the graph dictionary, but also generate an imprint in an additional layer of the simulation grid. During growth, each process checks for the presence of existing edges by generating a view in this grid. If there is an edge in the vicinity, it can be looked up in the dictionary using its identifier from the simulation grid. To additionally reduce the number of collision calculations between actively moving cones, a Voronoi tessellation is performed for all growing edges to cluster neighbouring cones within a Delaunay distance l_d. Only those agents that are able to interact during the following l_d-steps have to communicate during these steps, while all clusters are independent from each other and can be updated in parallel. The clustering step is repeated after l_d steps. In Figure 5, a 2-dimensional clustering is shown as an example. All agents with overlapping blue circles can interact and are part of the same cluster.

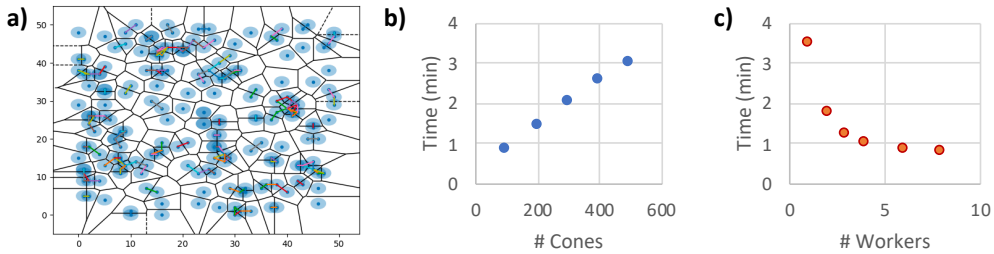

Fig 5. Clustering and performance. In (a), a 2-dimensional illustration of the clustering scheme to reduce the number of collision detections is shown for illustration. Blue dots correspond to active growth processes, and only processes with overlapping light-blue circles can interact. A Voronoi tessellation of the simulation volume is performed for all growing edges to cluster all neighbouring cones within a Delaunay distance l_d. Only agents that can interact during the following l_d-steps have to communicate during these steps, while all clusters are independent from each other and can be updated in parallel. In (b) and (c), the scaling of the simulation time with the number of growth cones and worker processes is shown.

All edges and nodes are instances of their respective classes, too, with the attributes shown in Table 4. The framework was implemented in Python 3 using *numpy* [45, 46]. The network is directly converted into a networkx graph for further processing and analysis. On a 8-core Intel Xeon 6134 3.2 GHz machine with 64 GB RAM, running a network simulation with 100 growth cones in a 256x256x256 tissue volume for 50 steps takes 60 seconds. The scaling of the simulation time with the number of growth cones and worker processes is shown in Figure 5. Source code, documentation and example configurations of our computational model are available at `https://github.com/CIA-CCTB/pythrahyper_net`.

Applications

We used our model to simulate the development of two biological network systems: the osteocyte lacuno-canalicular system in bone [14, 47, 48], and the sensory nervous system in Zebrafish [49, 50]. These two systems are prime examples where the final network architecture depends on the interplay of genetically encoded cell behaviour and the complex structured tissue environment.

The osteocyte lacuno-canalicular network (OLCN) develops during the deposition of new bone tissue by bone-forming cells called osteoblasts. Some of these cells get encased

Table 4. Edge and node object attributes

Edge attributes	**Type**	**Description**
Position list	array $[[x, y, z]_i, .., [x, y, z]_n]$	Position memory of all points on edge
Current nodes	list[str]	Two nodes connected by the edge
Constructor Cone	int	ID of the edge's constructor cone
flavor, edge number	int	ID and edge number
Node attributes	**Type**	textbfDescription
Position List	array $[[x, y, z]]$	Current node position
Edge List	list[str]	List with the IDs of all connected edges

Table 4: Internal attributes of nodes and edges, data types, and description.

in the newly deposited collagenous bone tissue as it slowly mineralizes, and differentiate into osteocytes. Fully differentiated osteocytes reside in small cavities (lacunae) inside the mineralized bone matrix. Their filopodia-like cell processes connect to each other and to blood vessels, forming a dense network of small channels (canaliculi) in the bone matrix. The architecture of the OLCN has been imaged quantitatively e.g. using confocal [7] and electron microscopy [51] or X-ray imaging [52], but the details of the process of network development remain largely unknown. Cell-matrix interactions as well as soluble cues by nearby cells and blood vessels likely play a role. In fibrolamellar and osteonal bone, the OLCN is more aligned and organized compared to woven bone [53], resulting in more optimized transport properties. This is related to the degree of organization and alignment of the extracellular matrix [54]. Our simulation framework can be used to study the influence of different factors such as matrix alignment and soluble signals on the resulting network topology of the OLCN. In Figure 6 a-b, we show two representative simulations of the osteocyte network with identical cell positions, but different degrees of matrix organization representing highly aligned (fibrolamellar) and unorganized (woven) bone matrix. The number of osteocyte processes, branching probability and persistence length were chosen using experimentally measured parameters reported in [14].

The second application example is the development of the sensory nervous system in the vertebrate model organism zebrafish (*Danio rerio*). During development, peripheral sensory axons grow from the spinal chord, arborize and innervate the skin, forming a dense neural network [49]. The navigation of the growth cones is a delicate interplay of attractive soluble factors, repulsive interaction, and physical guidance by the shape and tissue structure of the embryo. Static imaging of the final network reveals the structure, but capturing the transient dynamics of the process requires sophisticated time-lapse imaging at subcellular resolution [50, 55]. Our computational model ideally complements live imaging of neural development: it can be used to make specific prediction about the effects of changes in cellular behaviour and sensitivity, which can then be tested experimentally. Likewise, experimentally observed variations in network growth dynamics can be linked to specific cellular changes using computer simulations. In Figure 6c, we demonstrate the growth of a network where growth cones emanate from a spinal cord-like region at the bottom of a curved structure along a constant attractive gradient.

Discussion

We developed a novel agent-based framework to simulate the growth of networks in three-dimensional space. The outgrowth of individual processes follows a 3D random walk with memory (correlation) and directional bias due to interactions with the environment. This

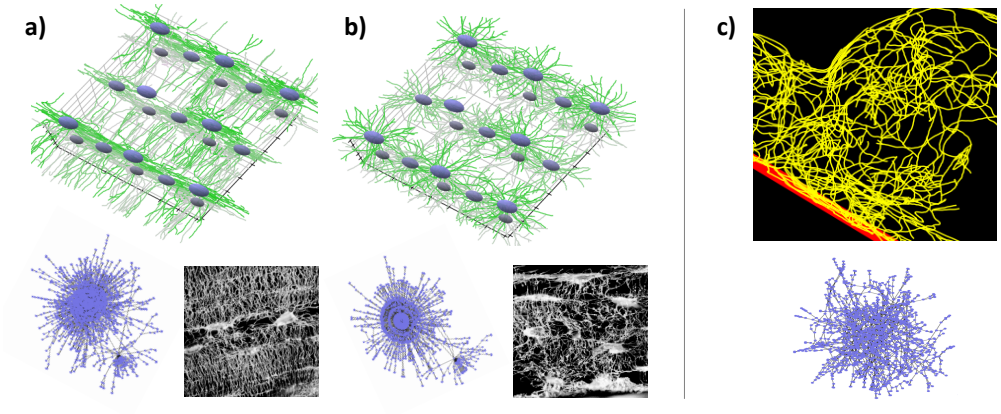

Fig 6. Fig. 6: Example simulations of spatial biological network development in complex environments. The osteocyte lacuno-cancalicular system in fibrolamellar (a) and woven (b) bone, with identical cell positions (blue) and starting conditions, but with different degrees of extracellular matrix organization. The alignment of the network (green) reflects the architecture of the extracellular matrix as a result of local alignment of the filopodia-like cell processes with the collagen fibers in the bone matrix during outgrowth. The graph representation of the networks is shown below left, and an experimental image of the respective bone types on the bottom right (own work). In (c), the sensory nervous system in zebrafish was simulated, inspired by the winner of the 2018 Nikon Small World Contest [56]. This network develops by outgrowth of axons from neurons in the spinal chord, guided by the curved tissue surface and attractive soluble signals. The corresponding network graph is shown below.

framework can be used to simulate the growth of biological networks on all scales from single cells to ecosystems, or of generic network development through interaction of autonomous agents with each other and with external physical and chemical cues. During simulation, the network is directly converted into a graph using the networkx library [57], which provides access to many quantitative and comparative measures of network topology.

Computer simulations of network growth date back at at least to the 1960s, and many improved theoretical models have been published since then. The key improvement over previous work is that the interaction with the environment is not modelled explicitly, e.g. in terms of hard-coded conditions, but through a generic mechanism based on angular probability density functions. Image volumes are used to store arbitrary chemical and physical properties of the growth environment. The corresponding signals acting on the growth cones of the network are derived from these images by calculating spatial image features such as gradient and structure tensor filters. While we used a fixed step length in our implementation, the growth velocity of individual agents can easily be varied by introducing a scaling factor for the Monte Carlo time step.

One class of biological networks where the interaction and feedback between invidiual growth cones and the microenvironment during growth determines the resulting network architecture are multicellular networks, such as neuronal networks in the brain or the osteocyte network in bone. In bone, different degrees of tissue organization and the presence of soluble cues determines the connectivity and arrangement of the resulting network. With the framework presented here, the question can be investigated how local cellular response and resulting network topology depend on each other by conducting virtual experiments with varying parameters, which would not be possible in real experiments. The resulting theoretical understanding can then inform the design of guiding structures (scaffolds) to facilitate optimal network development in regenerating bone by providing the relevant physical

and chemical signals [58].

The growth of vascular and neuronal cell networks during embryonal development is another example where soluble cues, the geometry of the environment, and the interaction between nearby cells all play an important role [49]. Recent improvements of lightsheet imaging technology now allow to visualize the entire growth process with high spatial and temporal resolution [55]. Our framework predicts not only the outcome, but also the dynamics of this process, which allows to test specific hypotheses about the biological mechanisms that locally control this growth process. In the future, this might contribute to solving the question to what degree functional network architecture is encoded in the genome, or how the interactions and mechanochemical feedback loops between cells and the environment during growth determine the resulting tissue organization. Another interesting example is the role of curvature for tissue growth and organization [59]. With our framework, it will be possible to systematically vary the curvature of growth surfaces for networks while including other relevant biological and physical signals in the same simulation framework.

A very interesting related field is the exploratory growth of plants guided by pairwise interactions, tropic reponses to signals (e.g. light), and nastic (e.g. helical) movements. Recently, a computational model was introduced to model the dynamics of such sensory-growth systems [60, 61], taking into account the mechanical properties of the growing system. Such a framework offers interesting opportunities not only to understand biological control principles, but also for designing self-growing artificial systems. It would be interesting to see how this approach can be extended towards the development of functional network architectures.

While we developed our framework with network growth in mind, it can also be turned around and used to find and trace network structures in noisy image volumes by treating them as guiding signals for growth. Many approaches exist to trace filaments [62, 63], but they often have difficulties with branching structures. By simulating multiple growth processes either directly on image data or e.g. on probability maps predicted by convolutional neural networks, our framework might be able to find also highly branching and irregular structures.

Network growth as defined here is a parallel process by definition and thus can be computed in a distributed manner. We describe an efficient strategy for parallelization while taking into account the interaction between neighbouring growth cones. Future improvements could make use of the massively parallel processing power of graphical processing units.

Conclusion

We developed a probabilistic agent-based model to describe individual growth processes as biased, correlated random motion with rules for branching, bifurcation, merging and termination. Using directional statistics, the influence of external cues on the growth process is obtained directly from real image data. Our tool allows to study the relationship between biological growth parameters and macroscopic function, and can generate plausible network graphs that take local feedback into account as basis for comparative studies using graph-based methods. Our approach is not limited to a specific type of network, includes a thorough treatment of probabilities, and can easily include arbitrary external constraints. We implemented our model in python and make it freely available as a computational framework that allows to perform simulations for diverse types of biological networks on all scales.

Acknowledgments

Computational work was performed using the High-Performance Computing Cloud of Würzburg University (DFG project 327497565).

References

1. Barthélemy M. Morphogenesis of Spatial Networks. Lecture Notes in Morphogenesis. Springer International Publishing; 2018. Available from: https://www.springer.com/de/book/9783319205649.

2. Kaiser M. Mechanisms of Connectome Development. Trends in Cognitive Sciences. 2017 Sep;21(9):703–717.

3. Maskery S, Shinbrot T. Deterministic and stochastic elements of axonal guidance. Annual Review of Biomedical Engineering. 2005;7:187–221.

4. Chédotal A, Richards LJ. Wiring the Brain: The Biology of Neuronal Guidance. Cold Spring Harbor Perspectives in Biology. 2010 Jun;2(6). Available from: https://www.ncbi.nlm.nih.gov/pmc/articles/PMC2869517/.

5. Banerjee S, Gardel ML, Schwarz US. The Actin Cytoskeleton as an Active Adaptive Material. Annual Review of Condensed Matter Physics. 2020;11(1):421–439. _eprint: https://doi.org/10.1146/annurev-conmatphys-031218-013231. Available from: https://doi.org/10.1146/annurev-conmatphys-031218-013231.

6. Secomb TW, Alberding JP, Hsu R, Dewhirst MW, Pries AR. Angiogenesis: An Adaptive Dynamic Biological Patterning Problem. PLOS Computational Biology. 2013 Mar;9(3):e1002983. Available from: http://journals.plos.org/ploscompbiol/article?id=10.1371/journal.pcbi.1002983.

7. Kerschnitzki M, Kollmannsberger P, Burghammer M, Duda GN, Weinkamer R, Wagermaier W, et al. Architecture of the osteocyte network correlates with bone material quality. Journal of Bone and Mineral Research: The Official Journal of the American Society for Bone and Mineral Research. 2013 Aug;28(8):1837–1845.

8. Jones J. Characteristics of pattern formation and evolution in approximations of Physarum transport networks. Artificial Life. 2010;16(2):127–153.

9. Bebber DP, Hynes J, Darrah PR, Boddy L, Fricker MD. Biological solutions to transport network design. Proceedings Biological Sciences. 2007 Sep;274(1623):2307–2315.

10. Duran-Nebreda S, Bassel GW. Bridging Scales in Plant Biology Using Network Science. Trends in Plant Science. 2017 Dec;22(12):1001–1003. Publisher: Elsevier. Available from: https://www.cell.com/trends/plant-science/abstract/S1360-1385(17)30216-9.

11. Eichler K, Li F, Litwin-Kumar A, Park Y, Andrade I, Schneider-Mizell CM, et al. The complete connectome of a learning and memory centre in an insect brain. Nature. 2017 Aug;548(7666):175–182. Available from: https://www.nature.com/articles/nature23455.

12. Meinertzhagen IA. Of what use is connectomics? A personal perspective on the Drosophila connectome. Journal of Experimental Biology. 2018 May;221(10):jeb164954. Available from: http://jeb.biologists.org/content/221/10/jeb164954.

13. Yan G, Vértes PE, Towlson EK, Chew YL, Walker DS, Schafer WR, et al. Network control principles predict neuron function in the Caenorhabditis elegans connectome. Nature. 2017 Oct;advance online publication. Available from: http://www.nature.com/nature/journal/vaop/ncurrent/full/nature24056.html?WT.ec_id=NATURE-20171019&spMailingID=55167568&spUserID=OTMzMjIzOTczNQS2&spJobID=1263146646&spReportId=MTI2MzE0NjY0NgS2.

14. Buenzli PR, Sims NA. Quantifying the osteocyte network in the human skeleton. Bone. 2015 Jun;75:144–150. Available from: http://www.sciencedirect.com/science/article/pii/S8756328215000617.

15. Novkovic M, Onder L, Bocharov G, Ludewig B. Topological Structure and Robustness of the Lymph Node Conduit System. Cell Reports. 2020 Jan;30(3):893–904.e6. Available from: https://www.cell.com/cell-reports/abstract/S2211-1247(19)31727-9.

16. Erdös P, Rényi A. On random graphs. I. Publicationes Mathematicae Debrecen. 1959;6:290–297. Available from: https://mathscinet.ams.org/mathscinet-getitem?mr=0120167.

17. Watts DJ, Strogatz SH. Collective dynamics of 'small-world' networks. Nature. 1998 Jun;393:440–442. Available from: http://adsabs.harvard.edu/abs/1998Natur.393..440W.

18. Comin C, da F Costa L. Spatial Networks: When Topology Meets Geometry (CDT-3). ResearchGate; 2018.

19. Kaiser M, Hilgetag CC. Spatial growth of real-world networks. Physical Review E. 2004 Mar;69(3):036103. Available from: https://link.aps.org/doi/10.1103/PhysRevE.69.036103.

20. Cohen D. Computer Simulation of Biological Pattern Generation Processes. Nature. 1967 Oct;216(5112):246–248. Available from: https://www.nature.com/articles/216246a0.

21. Zitin A, Gorowara A, Squires S, Herrera M, Antonsen TM, Girvan M, et al. Spatially embedded growing small-world networks. Scientific Reports. 2014 Nov;4:7047. Available from: https://www.nature.com/articles/srep07047.

22. Nicosia V, Vértes PE, Schafer WR, Latora V, Bullmore ET. Phase transition in the economically modeled growth of a cellular nervous system. Proceedings of the National Academy of Sciences. 2013 May;110(19):7880–7885. Available from: http://www.pnas.org/content/110/19/7880.

23. Cuntz H, Forstner F, Borst A, Häusser M. One Rule to Grow Them All: A General Theory of Neuronal Branching and Its Practical Application. PLOS Computational Biology. 2010 May;6(8):e1000877. Available from: http://journals.plos.org/ploscompbiol/article?id=10.1371/journal.pcbi.1000877.

24. Ronellenfitsch H, Katifori E. Global Optimization, Local Adaptation, and the Role of Growth in Distribution Networks. Physical Review Letters. 2016 Sep;117(13):138301. ArXiv: 1606.00331. Available from: http://arxiv.org/abs/1606.00331.

25. Zubler F, Hauri A, Pfister S, Bauer R, Anderson JC, Whatley AM, et al. Simulating Cortical Development as a Self Constructing Process: A Novel Multi-Scale Approach Combining Molecular and Physical Aspects. PLOS Computational Biology. 2013 Aug;9(8):e1003173. Available from: http://journals.plos.org/ploscompbiol/article?id=10.1371/journal.pcbi.1003173.

26. Koene RA, Tijms B, van Hees P, Postma F, de Ridder A, Ramakers GJA, et al. NETMORPH: A Framework for the Stochastic Generation of Large Scale Neuronal Networks With Realistic Neuron Morphologies. Neuroinformatics. 2009 Sep;7(3):195–210. Available from: https://doi.org/10.1007/s12021-009-9052-3.

27. Gaiselmann G, Thiedmann R, Manke I, Lehnert W, Schmidt V. Stochastic 3D modeling of fiber-based materials. Computational Materials Science. 2012 Jun;59:75–86. Available from: http://www.sciencedirect.com/science/article/pii/S0927025612001267.

28. Hannezo E, Scheele CLGJ, Moad M, Drogo N, Heer R, Sampogna RV, et al. A Unifying Theory of Branching Morphogenesis. Cell. 2017 Sep;171(1):242–255.e27. Available from: http://www.sciencedirect.com/science/article/pii/S0092867417309510.

29. Codling EA, Plank MJ, Benhamou S. Random walk models in biology. Journal of the Royal Society Interface. 2008 Aug;5(25):813–834. Available from: https://www.ncbi.nlm.nih.gov/pmc/articles/PMC2504494/.

30. Risken H, Frank T. The Fokker-Planck Equation: Methods of Solution and Applications. 2nd ed. Springer Series in Synergetics. Berlin Heidelberg: Springer-Verlag; 1996. Available from: https://www.springer.com/de/book/9783540615309.

31. Lemons DS, Gythiel A. Paul Langevin's 1908 paper "On the Theory of Brownian Motion" ["Sur la théorie du mouvement brownien," C. R. Acad. Sci. (Paris) 146, 530–533 (1908)]. American Journal of Physics. 1997 Nov;65(11):1079–1081. Available from: https://aapt.scitation.org/doi/10.1119/1.18725.

32. Patlak CS. Random walk with persistence and external bias. The bulletin of mathematical biophysics. 1953 Sep;15(3):311–338. Available from: https://doi.org/10.1007/BF02476407.

33. Boas ML, Romain JE. Mathematical Methods in the Physical Sciences. Physics Today. 2009 Jan;20(6):81. Publisher: American Institute of PhysicsAIP. Available from: https://physicstoday.scitation.org/doi/abs/10.1063/1.3034374.

34. Koenderink JJ. The structure of images. Biological Cybernetics. 1984 Aug;50(5):363–370. Available from: https://doi.org/10.1007/BF00336961.

35. TschumperlÉ D. Fast Anisotropic Smoothing of Multi-Valued Images using Curvature-Preserving PDE's. International Journal of Computer Vision. 2006 Jun;68(1):65–82. Available from: https://doi.org/10.1007/s11263-006-5631-z.

36. Weickert J. A review of nonlinear diffusion filtering. In: ter Haar Romeny B, Florack L, Koenderink J, Viergever M, editors. Scale-Space Theory in Computer Vision. Lecture Notes in Computer Science. Berlin, Heidelberg: Springer; 1997. p. 1–28.

37. Fisher NI, Lewis T, Embleton BJJ. Statistical Analysis of Spherical Data. Cambridge: Cambridge University Press; 1987. Available from: https://www.cambridge.org/core/books/statistical-analysis-of-spherical-data/CCFE72380FB730E48080D7596135A363.

38. Bingham C. An Antipodally Symmetric Distribution on the Sphere. The Annals of Statistics. 1974;2(6):1201–1225. Available from: https://www.jstor.org/stable/2958339.

39. Kent JT. The Fisher-Bingham Distribution on the Sphere. Journal of the Royal Statistical Society Series B (Methodological). 1982;44(1):71–80. Available from: https://www.jstor.org/stable/2984712.

40. Mardia KV, Jupp PE. Directional Statistics. John Wiley & Sons; 2009.

41. Kent JT, Ganeiber AM, Mardia KV. A new method to simulate the Bingham and related distributions in directional data analysis with applications. arXiv:13108110 [math, stat]. 2013 Oct;ArXiv: 1310.8110. Available from: http://arxiv.org/abs/1310.8110.

42. Paine PJ, Preston SP, Tsagris M, Wood ATA. An elliptically symmetric angular Gaussian distribution. Statistics and Computing. 2018 May;28(3):689–697. Available from: https://doi.org/10.1007/s11222-017-9756-4.

43. Kuhn W. Über die Gestalt fadenförmiger Moleküle in Lösungen. Kolloid-Zeitschrift. 1934 Feb;68(1):2–15. Available from: https://doi.org/10.1007/BF01451681.

44. Takács L. Non-Markovian Processes. In: Takács L, editor. Stochastic Process: Problems and Solutions. Methuen's Monographs on Applied Probability and Statistics. Dordrecht: Springer Netherlands; 1966. p. 46–62. Available from: https://doi.org/10.1007/978-94-011-6020-9_4.

45. Virtanen P, Gommers R, Oliphant TE, Haberland M, Reddy T, Cournapeau D, et al. SciPy 1.0: fundamental algorithms for scientific computing in Python. Nature Methods. 2020 Mar;17(3):261–272. Number: 3 Publisher: Nature Publishing Group. Available from: https://www.nature.com/articles/s41592-019-0686-2.

46. van der Walt S, Colbert SC, Varoquaux G. The NumPy Array: A Structure for Efficient Numerical Computation. Computing in Science Engineering. 2011 Mar;13(2):22–30. Conference Name: Computing in Science Engineering.

47. Bonewald LF. The amazing osteocyte. Journal of Bone and Mineral Research: The Official Journal of the American Society for Bone and Mineral Research. 2011 Feb;26(2):229–238.

48. Weinkamer R, Kollmannsberger P, Fratzl P. Towards a Connectomic Description of the Osteocyte Lacunocanalicular Network in Bone. Current Osteoporosis Reports. 2019 Aug;17(4):186–194. Available from: https://doi.org/10.1007/s11914-019-00515-z.

49. Roy S. Development of the zebrafish nervous system: Mechanisms of cellfate specification and axonal pathfinding in the central nervous system and periphery. Current Science. 1994;66(9):629–633. Publisher: Current Science Association. Available from: https://www.jstor.org/stable/24098781.

50. Rieger S, Wang F, Sagasti A. Time-lapse imaging of neural development: Zebrafish lead the way into the fourth dimension. Genesis (New York, NY : 2000). 2011 Jul;49(7):534–545. Available from: https://www.ncbi.nlm.nih.gov/pmc/articles/PMC3132295/.

51. Schneider P, Meier M, Wepf R, Müller R. Towards quantitative 3D imaging of the osteocyte lacuno-canalicular network. Bone. 2010 Nov;47(5):848–858.

52. Pacureanu A, Langer M, Boller E, Tafforeau P, Peyrin F. Nanoscale imaging of the bone cell network with synchrotron X-ray tomography: optimization of acquisition setup. Medical Physics. 2012 Apr;39(4):2229–2238.

53. Kollmannsberger P, Kerschnitzki M, Repp F, Wagermaier W, Weinkamer R, Peter Fratzl. The small world of osteocytes: connectomics of the lacuno-canalicular network in bone. New Journal of Physics. 2017;19(7):073019. Available from: http://stacks.iop.org/1367-2630/19/i=7/a=073019.

54. Repp F, Kollmannsberger P, Roschger A, Berzlanovich A, Gruber GM, Roschger P, et al. Coalignment of osteocyte canaliculi and collagen fibers in human osteonal bone. Journal of Structural Biology. 2017 Sep;199(3):177–186.

55. Huisken J, Swoger J, Bene FD, Wittbrodt J, Stelzer EHK. Optical Sectioning Deep Inside Live Embryos by Selective Plane Illumination Microscopy. Science. 2004 Aug;305(5686):1007–1009. Publisher: American Association for the Advancement of Science Section: Report. Available from: https://science.sciencemag.org/content/305/5686/1007.

56. Developing Sensory Nervous System of a Zebrafish Wins 2018 Nikon Small World in Motion Competition | News;. Library Catalog: www.nikonsmallworld.com. Available from: https://www.nikonsmallworld.com/news/developing-sensory-nervous-system-of-a-zebrafish-wins-2018-nikon-small-wo

57. Hagberg AA, Schult DA, Swart PJ. Exploring Network Structure, Dynamics, and Function using NetworkX. Proceedings of the 7th Python in Science Conference. 2008;p. 11 – 15.

58. Bidan CM, Kommareddy KP, Rumpler M, Kollmannsberger P, Fratzl P, Dunlop JWC. Geometry as a Factor for Tissue Growth: Towards Shape Optimization of Tissue Engineering Scaffolds. Advanced Healthcare Materials. 2013;2(1):186–194. _eprint: https://onlinelibrary.wiley.com/doi/pdf/10.1002/adhm.201200159. Available from: https://onlinelibrary.wiley.com/doi/abs/10.1002/adhm.201200159.

59. Kollmannsberger P, Bidan CM, Dunlop JWC, Fratzl P. The physics of tissue patterning and extracellular matrix organisation: how cells join forces. Soft Matter. 2011 Oct;7(20):9549–9560. Publisher: The Royal Society of Chemistry. Available from: https://pubs.rsc.org/en/content/articlelanding/2011/sm/c1sm05588g.

60. Bastien R, Porat A, Meroz Y. Towards a framework for collective behavior in growth-driven systems, based on plant-inspired allotropic pairwise interactions. Bioinspiration & Biomimetics. 2019 Aug;14(5):055004. Available from: https://iopscience.iop.org/article/10.1088/1748-3190/ab30d3/meta.

61. Porat A, Tedone F, Palladino M, Marcati P, Meroz Y. A general 3D model for growth dynamics of sensory-growth systems: from plants to robotics. bioRxiv. 2020 Apr;p. 2020.04.21.053033. Publisher: Cold Spring Harbor Laboratory Section: New Results. Available from: https://www.biorxiv.org/content/10.1101/2020.04.21.053033v1.

62. Türetken E, Benmansour F, Andres B, Głowacki P, Pfister H, Fua P. Reconstructing Curvilinear Networks Using Path Classifiers and Integer Programming. IEEE Transactions on Pattern Analysis and Machine Intelligence. 2016 Dec;38(12):2515–2530.

63. Acciai L, Soda P, Iannello G. Automated Neuron Tracing Methods: An Updated Account. Neuroinformatics. 2016 Oct;14(4):353–367. Available from: https://doi.org/10.1007/s12021-016-9310-0.